Estimating global ammonia (NH_3) emissions based on IASI observations from 2008 to 2018

Zhenqi Luo[1, 2], Yuzhong Zhang[1, 2, *], Wei Chen[1, 2], Martin van Damme[3, 4], Pierre-François Coheur[3], Lieven Clarisse[3]

[1]Key Laboratory of Coastal Environment and Resources of Zhejiang Province, School of Engineering, Westlake University, Hangzhou, Zhejiang Province, 310024, China
[2]Institute of Advanced Technology, Westlake Institute for Advanced Study, Hangzhou, Zhejiang Province, 310024, China
[3]Université libre de Bruxelles (ULB), Spectroscopy, Quantum Chemistry and Atmospheric Remote Sensing (SQUARES), Brussels, Belgium
[4]BIRA-IASB - Belgian Institute for Space Aeronomy, Brussels, Belgium

Correspondence to: Y. Zhang (zhangyuzhong@westlake.edu.cn), Z. Luo (zl725@cornell.edu)

Abstract. Emissions of ammonia (NH_3) to the atmosphere impact human health, climate, and ecosystems through their critical contributions to secondary aerosol formation. Estimation of NH_3 emissions is associated with large uncertainties because of inadequate knowledge about agricultural sources. Here, we use satellite observations from the Infrared Atmospheric Sounding Interferometer (IASI) and simulations from the GEOS-Chem model to constrain global NH_3 emissions over the period of 2008-2018. We update the prior NH_3 emission fluxes with the ratio between biases in simulated NH_3 concentrations and effective NH_3 lifetimes against the loss of the NH_x family. In contrast to about a factor of two discrepancies between top-down and bottom-up emissions found in previous studies, our method results in a global land NH_3 emission of 78 (70-92) Tg a^{-1}, ~30 % higher than the bottom-up estimates. Regionally, we find that the bottom-up inventory underestimates NH_3 emissions over South America and tropical Africa by 60-70 %, indicating under-representation of agricultural sources in these regions. We find a good agreement within 10 % between bottom-up and top-down estimates over the U.S., Europe, and eastern China. Our results also show significant increases in NH_3 emissions over India (13 % decade^{-1}), tropical Africa (33 % decade^{-1}), and South America (18 % decade^{-1}) during our study period, consistent with the intensifying agricultural activities in these regions in the past decade. We find that inclusion of sulfur dioxide (SO_2) column observed by satellite is crucial for more accurate inference of NH_3 emission trends over important source regions such as India and China where SO_2 emissions have changed rapidly in recent years.

1 Introduction

Emissions of ammonia (NH_3) to the atmosphere have critical implications for human health, climate, and ecosystems. As the main alkaline gas, NH_3 reacts with acidic products from precursors such as nitrogen oxides (NO_x) and sulfur dioxide (SO_2) to form fine particulate matter, which is a well-documented risk factor for human health, causing great welfare loss globally

(Erisman 2021; Gu et al., 2021). Particulate matter also affects the Earth's radiative balance by directly scattering incoming radiation (Ma et al., 2012) and indirectly as cloud condensation nuclei (Höpfner et al., 2019). Additionally, both gas-phase ammonia (NH_3) and aerosol-phase ammonium (NH_4^+) can deposit onto the surface of land and water through dry and wet processes, and are associated with soil acidification (Zhao et al., 2009), ecosystem eutrophication (Dirnböck et al., 2013), biodiversity loss (Stevens et al., 2010), and cropland nitrogen uptake (Liu et al., 2013).

NH_3 is emitted from a variety of anthropogenic and natural sources, including agriculture, industry, fossil fuel combustion, biomass burning, natural soils, ocean, and wild animals (Behera et al., 2013). Among these, agricultural activities, mainly livestock manure management and mineral fertilizer application, are the most important NH_3 sources, which account for ~70% of the total NH_3 emissions globally (Bouwman et al., 1997; Sutton et al., 2013). NH_3 emissions can be estimated with a bottom-up approach based on information of emission activities and emission factors (Hoesly et al., 2018; Crippa et al., 2021). However, bottom-up estimates of NH_3 emissions are generally thought to be uncertain, relative to other pollutants that are mainly from fossil fuel combustion sources (e.g., NO_x, CO). One of the challenges is that the intensity of agricultural NH_3 emissions, emission factors, either from livestock or fertilizer, depends strongly on management and farming practices, but this information is usually not widely available (Zhang et al., 2017). Furthermore, microbial activities that are responsible for agricultural NH_3 emissions are highly variable and has a complex dependence on environmental conditions, which is often inadequately captured by bottom-up approaches (Behera et al., 2013; Vira et al., 2021). In many cases, emission factors used in bottom-up modelling are based on local studies that are not representative for the diversity of conditions and are not dependent on meteorological parameters.

Top-down analyses of atmospheric observations (e.g., NH_3 concentrations or NH_4^+ depositional fluxes) provide an alternative constraint on NH_3 emissions. For example, observations of NH_3 concentrations and NH_4^+ deposition fluxes from surface networks can be used to infer regional NH_3 emission fluxes (e.g., Paulot et al., 2014). However, surface sites are often sparse, especially in developing continents such as Africa and South America, limiting our capability to constrain NH_3 emissions globally. The advent of satellite observations makes it possible to investigate long-term spatially resolved NH_3 emissions from national, continental, to global scales. Van Damme et al. (2018) reported large NH_3 point sources across the globe that are detected by the Infrared Atmospheric Sounding Interferometer (IASI) instrument but missing in the bottom-up inventories. Studies have also applied satellite data (e.g., IASI and Cross-track Infrared Sounder (CrIS)) to study NH_3 emissions from important source regions, including the U.S. (Cao et al., 2020; Chen et al., 2021b), China (Zhang et al., 2018), and Europe (Marais et al., 2021; van der Graaf et al., 2021). These regional studies show 20 % to 50 % differences between top-down and bottom-up estimates of NH_3 emissions.

Compared to regional analyses, long-term global analyses of NH_3 emissions based on satellite observations are relatively scarce (e.g., Evangeliou et al., 2021). This is partly because of the computational challenges arising from a full-fledged inversion for a long period of time and over large spatial extents. In a recent study, Evangeliou et al. (2021) proposed a fast top-down method, in which NH_3 emissions are computed as the ratio between NH_3 column observations and NH_3 lifetime. This method relies on NH_3 lifetime diagnosed from a chemical transport model (CTM) and assumes a local mass balance.

67 Their analysis found a global NH_3 emission of around 180 Tg a^{-1}, which is roughly triple the widely used bottom-up

68 estimates (e.g., 62 Tg a^{-1} by the Community Emission Data System, CEDS). This large upward adjustment, if true, would

69 have huge implications for global reactive nitrogen cycles and indicate that our current understanding of global NH_3

70 emissions is seriously flawed.

71 In this paper, we examine if the large discrepancy between the bottom-up and top-down estimates is due to the methodology.

72 We refine the fast top-down approach by improving NH_3 lifetime diagnosis and partially accounting for the transport

73 contributions. We develop a series of data filtering procedures to exclude results that are not sufficiently constrained by

74 observations or affected by large deviations from the assumption of the fast top-down method. We apply the updated method

75 to IASI observations to derive the global distribution of NH_3 emissions fluxes from 2008 to 2018, and examine the impact of

76 the improved method on global NH_3 emission inferences.

77 **2 Methods**

78 **2.1 IASI observations**

79 We use 2008-2018 reanalyzed daily NH_3 total column retrievals (ANNI-NH_3-v3R) from the IASI on board Metop-A. The

80 IASI instrument measures the infrared radiation (645–2760 cm^{-1}) from Earth's surface and the atmosphere with a circular 12

81 km footprint at nadir (Clerbaux et al., 2009; Van Damme et al., 2017). The retrieval algorithm calculates the hyperspectral

82 range index from IASI spectra measurements (Van Damme et al. 2014) and converts it to the NH_3 total column density via

83 an artificial neural network (Whitburn et al., 2016; Franco et al., 2018). The retrieval uses consistent meteorological data

84 from the ERA5 reanalysis, so it is suitable for the analyses of inter-annual variability and long-term trends (Hersbach et al.,

85 2020). The ANNI-NH_3-v3R product, has been validated against in situ measurements and is shown to have a good regional

86 correlation (Guo et al., 2021; Van Damme et al., 2021). The dataset has been used in previous studies to estimate NH_3

87 emissions globally (e.g., Evangeliou et al., 2021) and regionally (e.g., Chen et al., 2021b; Marais et al., 2021).

88 Here we only use morning NH_3 data (around 9:30 local solar time) though IASI provides global coverage twice daily,

89 because of the better precision of morning observations resulting from favourable thermal contrast conditions (Clarisse et al.

90 2010). We filter out data with a cloud fraction greater than 10 % (Van Damme et al., 2018) and a skin temperature below

91 263 K (Van Damme et al., 2014). The skin temperature dataset is from ERA5 (Hersbach et al., 2020). To compare with

92 simulated NH_3 columns (see **Sect. 2.2**), we regrid and average monthly IASI NH_3 observations over land on the GEOS-

93 Chem 4° × 5° grid (**Fig. 1a**). To reduce uncertainty from sparse sampling, we further exclude grid cells with the number of

94 successful retrievals less than 800 in a month. We also test the choices of the threshold for 400 and 1200 per month in the

95 sensitivity calculations (**Table 1**, line 5-6). This criterion affects mainly high latitudes during wintertime, where snow

96 surfaces make it unfavourable for infrared measurements (**Fig. S1**).
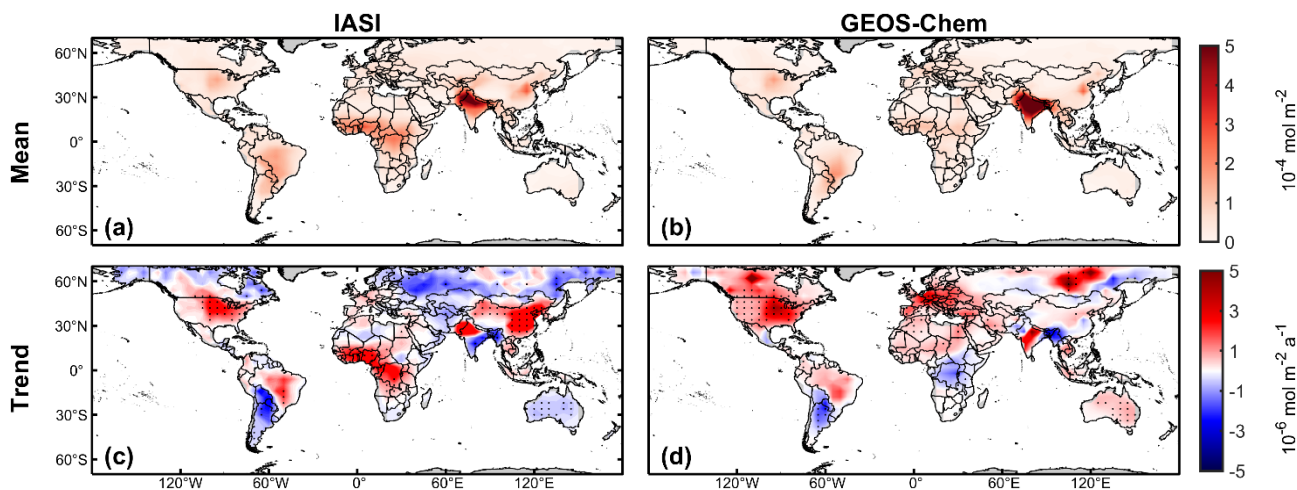
Figure 1. Spatial distribution of (a, c) IASI and (b, d) GEOS-Chem NH₃ column concentrations. (a, b) Mean and (c, d) linear trends within the **70**°N-**70**°S during 2008-2018. Dots in (c) and (d) indicate that linear trends are significant at the 95 % confidence levels. Linear trends are computed from the time series of annual averages.

2.2 GEOS-Chem simulations

We use the GEOS-Chem CTM v12.9.3 (10.5281/zenodo.3974569) to simulate global NH₃ concentrations. The GEOS-Chem model, driven by the MERRA-2 reanalyzed meteorology (Gelaro et al., 2017), simulates the tropospheric ozone–NOx–VOCs–aerosol chemistry at 4° × 5° resolution with 47 vertical layers (30 layers in the troposphere) (Bey et al., 2001; Park et al., 2004). The thermodynamic equilibrium between gas phase NH₃ and aerosol phase NH₄⁺ is explicitly simulated by the ISORROPIA-II module in GEOS-Chem (Fountoukis & Nenes, 2007). The model also simulates the wet and dry deposition of NH₃ and NH₄⁺, the terminal sinks of atmospheric NHₓ ($\equiv$ NH₃ + NH₄⁺). Dry deposition is represented with a resistances-in-series scheme (Wesely, 2007) and wet deposition includes scavenging in convective updrafts and in- and below-cloud scavenging from large-scale precipitation (Wang et al., 2011; Amos et al., 2012). Anthropogenic emissions of simulated chemicals including those of NH₃ are taken from a global emission inventory CEDS (Hoesly et al., 2018), overridden by regional inventories in Canada (Air Pollutant Emission Inventory, APEI), the United States (2011 National Emissions Inventory, NEI-2011), Asia (MIX-Asia v1.1) (Li et al., 2017), and Africa (DICE-Africa) (Eloise Marais and Christine Wiedinmyer, 2016). Such compiled anthropogenic emissions only include incomplete information on inter-annual trends because inventories are not all available throughout the whole period. Anthropogenic emissions are essentially invariant after 2013 in our setup (**Fig. S2**). The general lack of trends in SO₂ emissions in the simulation, if not accounted for, may cause biases in inferred trends over regions such as India and China where SO₂ emissions have changed rapidly (Sun et al., 2018; Qu et al., 2019; Chen et al., 2021a). Fire emissions are from Global Fire Emissions Database (GFED4) (van der Werf et al., 2017), and biogenic VOC emissions are from the Model of Emissions of Gases and Aerosols from Nature (MEGAN) (Guenther et al., 2012). Temporal (seasonal and inter-annual) variations in fire and biogenic emissions are resolved by the inventories. Hereafter, we refer to NH₃ prior bottom-up emissions from this set of inventories as BUE1. For comparison, we

122 also use another set of bottom-up inventories which consist of EDGARv5.0 for anthropogenic emissions
123 (https://data.jrc.ec.europa.eu/collection/edgar, last access: 8 March 2022, Crippa et al., 2020), GFAS for fire emissions
124 (CAMS, https://apps.ecmwf.int/datasets/data/cams-gfas/, last access: 8 March 2022) (minor natural emissions are the same
125 as BUE1), which we denote as BUE2.

126 The GEOS-Chem simulation is conducted from 2008 to 2018 with an additional 1-month spin-up starting from December
127 2007. We sample the simulated NH_3 and NH_4^+ concentration fields between 9:00 to 10:00 local solar time, approximately the
128 IASI morning overpass time. To compare with the IASI NH_3 columns, we integrate the vertical profiles of simulated NH_3
129 concentrations by layer thickness. We note that the ANNI-NH_3-v3R retrievalalgorithm does not provideinvolve averaging
130 kernels (Whitburn et al., 2016; Van Damme et al., 2021). However, Van Damme et al. (2018) reported the uncertainty in
131 different vertical profiles of individual NH_3 measurements to be 2 % $\pm$ 24 % (global average). Besides, weWe also archive
132 simulated depositional and transport rates for NH_3 and NH_4^+, which are used in emission fluxes estimation. In addition, we
133 perform GEOS-Chem simulations in selected years (2008, 2013, 2018) to examine the validation and consistency of our top-
134 down NH_3 emission estimates with the ground-based measurements and IASI observations.

135 **2.3 NH_3 emission fluxes estimation**

136 We compute NH_3 fluxes ($\hat{E}_{NH_3}$, in molecules m^{-2} s^{-1}) in land grid cells for individual months from 2008 to 2018. We update
137 the prior model emission fluxes ($E_{NH_3,mod}$, in molecules m^{-2} s^{-1}) with a correction term positively proportional to the
138 difference of observed ($C_{NH_3,obs}$, in molecules m^{-2}) and simulated ($C_{NH_3,mod}$, in molecules m^{-2}) monthly averaged NH_3 total
139 column densities and inversely proportional to the lifetime of NH_3 ($\tau_{NH_3,mod}$, in s):

$$\hat{E}_{NH_3} = E_{NH_3,mod} + \frac{C_{NH_3,obs} - C_{NH_3,mod}}{\tau_{NH_3,mod}}, \tag{1}$$

141 where $\tau_{NH_3,mod}$ is computed as the ratio of the simulated NH_3 column and the sum of simulated loss rate of the NH_x family
142 ($NH_x \equiv NH_3 + NH_4^+$) through the dry and wet depositions of NH_3 ($D_{NH_3,mod}$, in molecules m^{-2} s^{-1}) and NH_4^+ ($D_{NH_4^+,mod}$, in
143 molecules m^{-2} s^{-1}):

$$\tau_{NH_3,mod} = \frac{C_{NH_3,mod}}{D_{NH_3,mod} + D_{NH_4^+,mod}}. \tag{2}$$

145 Here we calculate the lifetime of NH_3 with the loss of the NH_x family rather than that of NH_3, because of the fast
146 thermodynamic equilibrium between gas-phase NH_3 and aerosol/aqueous-phase NH_4^+, which implies that the conversion
147 from NH_3 to NH_4^+ is not a terminal loss for NH_3 from the atmosphere. The NH_3 lifetime may be underestimated over source
148 regions and overestimated over remote regions, if NH_3 to NH_4^+ conversions are treated as a terminal loss as in Evangeliou et
149 al. (2021) rather than a partition within a chemical family (NH_x) as in **Eq. (2)**.

150 In addition, our method linearizes the column-emission relationship at prior emissions as opposed to zero emissions in the
151 previous method (e.g., Evangeliou et al., 2021). Here, the baseline NH_3 column ($C_{NH_3,mod}$) simulated by the GEOS-Chem

152 model explicitly accounts for the non-local contribution of transport, while the correction to prior emissions is done only

153 locally, that is, the difference between $C_{NH_3,obs}$ and $C_{NH_3,mod}$ is attributed only to errors in local emissions without

154 accounting for the sensitivity to emissions from other grid cells. This hybrid approach can partially include the non-local

155 contribution from transport but still keeps the computation tractable for a long-term study such as this study, striking a trade-

156 off between the computational efficiency of a local mass balance method (e.g., Van Damme et al., 2018; Evangeliou et al.,

157 2021) and the accuracy of a full-fledged inversion, such as the 4D-Var method (e.g., Cao et al., 2020; Chen et al., 2021b).

158 The errors arising from local correction of NH_3 emissions are expected to be small in most cases, because the NH_3 lifetime is

159 short relative to a typical transport time across a $4° \times 5°$ grid cell on which emissions are estimated. To identify cases when

160 this error is not negligible, we apply a monthly NH_x budget analysis based on the GEOS-Chem simulation and exclude grid

161 cells from our analysis where transport dominates over local prior emissions or depositions in the monthly NH_x budget

162 (Transport/Emission>1 or Transport/Deposition>1) (**Fig. S3**).

163 Because rapid changes in SO_2 emissions in eastern China and India, particularly after 2012, are not captured by our prior

164 simulation (**Fig. S2**), the estimation of NH_3 emission trends using **Eq. (1)** may be biased over these regions. To address this

165 issue, we further modify **Eq. (1)** to include observed trends in SO_2 column concentrations:

$$166 \qquad \hat{E}_{NH_3,SO_2-correct} = E_{NH_3,mod} + \frac{C_{NH_3,obs} - C_{NH_3,mod} + 2\omega C_{SO_4^{2-},mod}}{\tau_{NH_3,mod}}, \qquad (3)$$

167 where ω (%) is the fractional changes of average SO_2 columns relative to the baseline year (i.e., 2012) over China or India

168 and $C_{SO_4^{2-},mod}$ (molecules m^{-2} s^{-1}) is the simulated column densities of aerosol sulfate. Here, we specify a linear trend of -5 %

169 a^{-1} for eastern China and 5 % a^{-1} for India between 2012 and 2018, based on values derived from the ozone monitoring

170 instrument (OMI) and Ozone Mapping and Profiler Suite (OMPS) observations (Wang and Wang, 2020; Liu et al., 2018).

171 We also test the impact of the uncertainty in ω on trend inferences over China and India. The factor 2 accounts for the fact

172 that two molecules of NH_3 are required to neutralize one molecule of H_2SO_4. **Eq. (3)** only applies when NH_3 is in excess, a

173 condition usually met in eastern China and India but not necessarily elsewhere (Lachatre et al., 2019; Acharja et al., 2022).

174 Therefore, we only apply **Eq. (3)** to eastern China and India to understand the impact of changing SO_2 emissions on the

175 inference of NH_3 emission trends. To use SO_2 observations systematically in NH_3 emission estimations requires further

176 investigations.

177 **2.4 Uncertainty and sensitivity analysis**

178 We perform a series of perturbation and sensitivity experiments to assess the uncertainty of our estimates (**Table 1**. We

179 perturb $C_{NH_3,mod}$ and $\tau_{NH_3,mod}$ in **Eq. (1)**. The perturbations to $\tau_{NH_3,mod}$ are set to be 50 % and 200 % (**Table 1**, Line 1-2).

180 The perturbation to $C_{NH_3,mod}$ is set to be the standard deviation of monthly mean column concentrations ($\sigma_{C,obs}$) (**Table 1**,

181 Line 3-4), which is given by:

182
$$\sigma_{C,obs} = \sqrt{\frac{\sum_{i=1}^{i=n}(\sigma_i \times \Omega_i)^2}{n-1}}, \quad (4)$$

183 where Ω_i (in mol m^{-2}) is the ith NH$_3$ column measurement out of a total number of n observations in a grid cell during a

184 month and σ_i is the relative error. We then use $\Omega \pm \sigma_{C,obs}$ to evaluate the effect of measurement errors in emission estimates

185 (**Table 1**, Line 3-4). We compute results with alternative data filtering parameters (**Table 1**, Line 5-8), including the

186 thresholds to exclude grid cells when the number of observations is too small (**Table 1**, line 5-6) and the local mass balance

187 assumption is potentially invalid (**Table 1**, Line 7-8). We also test if our trend inferences over China and India using Eq. (3)

188 is sensitive to uncertainty in observed trends in SO$_2$ concentrations (ω).

189 **Table 1.** Uncertainty and sensitivity analyses of top-down NH$_3$ emissions. Annual averaged NH$_3$ emissions are summed over global land
190 areas for 2008–2018.

	Parameter perturbed	Average emission (Tg a^{-1})
0	None [a] (TDE)	78
1	Halved NH$_3$ lifetime[b]	92
2	Doubled NH$_3$ lifetime[c]	70
3	Upper IASI column error	83
4	Lower IASI column error	72
5	Number of retrievals > 400[d]	81
6	Number of retrievals > 1200[e]	74
7	Transport/Emission < 0.2[f]	72
8	Transport/Emission < 5[g]	84

191 [a]Excluding a grid cell if retrieval number is less than 800 during a month, or transport dominates over emissions or

192 depositions in the simulated monthly NH$_3$ budget.

193 [b-c]The lifetime is 50 % and 200 % of values from Eq. (1), respectively.

194 [d-e]Monthly retrieval number threshold for including a grid cell is set to be 400 and 1200, respectively.

195 [f-g]Local budget ratio the threshold for including a grid cell is set to be 0.2 and 5, respectively.

196 **3 Results and discussion**

197 **3.1 Observed and simulated NH$_3$ concentrations**

198 **Fig. 1a and 1b** plot observed and simulated NH$_3$ total column concentrations averaged over 2008-2018. The GEOS-Chem

199 simulation generally reproduces the global distribution of NH$_3$ concentrations observed by the IASI instrument. Good

200 agreements (i.e., difference < 10 %) are found in the U.S., Europe, and southern South America. Meanwhile, the GEOS-

201 Chem model underestimates NH_3 concentrations in eastern China, northern South America, and tropical Africa by 20-120 %,
202 and overestimates in southern India by around 50 %, indicating biases in NH_3 emissions over these regions.

203 **Fig. 1c and 1d** show 2008-2018 linear trends in NH_3 column concentrations derived from the IASI observations and the
204 GEOS-Chem simulations. The linear trends are computed based on the time series of annual averages. The IASI trends
205 shown in Fig. 1c are in general consistent with a recent analysis by Van Damme et al. (2021). IASI observes a positive NH_3
206 concentration trend of 2.9 % a^{-1} over the U.S., and this trend is well captured by GEOS-Chem. Similarly, the observation and
207 the simulation agree on a dipole pattern in South America (i.e., positive trend in Brazil and negative trend in Argentina).
208 Because anthropogenic emissions over this region are set to be invariant in our simulation (**Fig. S2**), this agreement suggests
209 that these trends are due to meteorological conditions and/or fire emissions, rather than changes in anthropogenic emissions.
210 The satellite also observes significant positive trends in NH_3 concentrations over China (5.2 % a^{-1}) and tropical Africa (2.0 %
211 a^{-1}), but these trends are not reproduced in the simulation (0.3 % a^{-1} for China and 0.2 % a^{-1} for tropical Africa). These
212 simulation-observation differences can not only reflect discrepancies in the trends of anthropogenic NH_3 emissions, but also
213 be attributed to uncaptured changes in SO_2 and/or NO_x emissions in these regions. We also find that a positive NH_3
214 concentration trend over Europe appears in the simulation (3.0 % a^{-1}) but is much weaker (1.0 % a^{-1}) in the observation,
215 suggesting decreasing emissions after 2013. Satellite data shows positive NH_3 concentration trends in north-western India
216 but negative trends in in south-eastern India which are not reproduced by the simulation, though these trends over India are
217 mostly insignificant (at the 95 % confidence level) except for a few grid cells in the Southeast. Strong GEOS-Chem trends in
218 eastern Canada and Siberia result from large wildfires that occurred in the latter part of the study period. IASI trends in
219 northern boreal regions are less robust because of noisy and sparse measurements over high latitudes (**Fig. S1** and **Fig. S3**)

220 **3.2 NH_3 emissions inferred from IASI observations**

221 **Fig. 2** shows the spatial distributions of NH_3 emission fluxes and their 2008–2018 linear trends inferred from IASI
222 observations using the method described in **Sect. 2.3**. **Fig. 3** plots annual time series aggregated for seven selected regions.
223 The top-down emission (TDE) estimates suggest upward adjustments in NH_3 emissions over South America (SA) by 62 %,
224 tropical Africa (TA) by 69 %, and Central Asia (CA) by 327 %, relative to the prior inventory (BUE1), but downward
225 adjustments in NH_3 emissions by 14 % in India Peninsula (IP) and by 33 % in Canada. After accounting for the contributions
226 from natural emissions including fires, we find that most of these biases in NH_3 emissions can be attributed to anthropogenic
227 sources, except for Canada where the underestimation appears to relate to fire emissions. This result reflects a general
228 inadequate representation of agricultural and industrial emissions from developing continents in current global emission
229 inventories. The TDE finds good agreements with the BUE1 (difference within 10 %) over the U.S., Europe (EU), eastern
230 China (EC) and Australia.
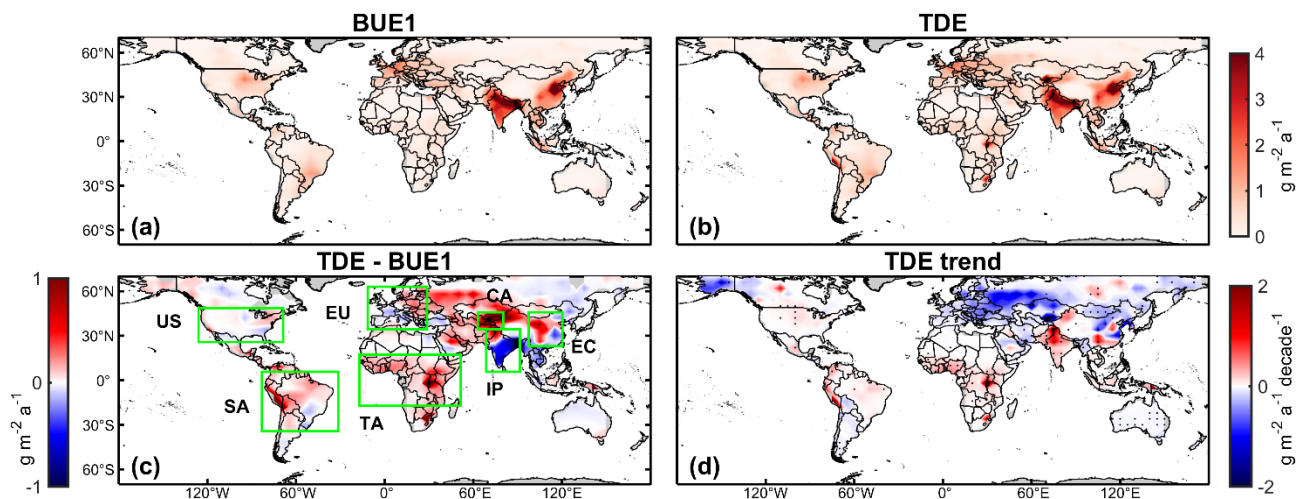
Figure 2. Spatial distribution of NH_3 emission fluxes during 2008-2018. (a) Bottom-up emissions (BUE1), (b) top-down emissions (TDE) inferred from IASI observations, (c) difference between TDE and BUE1 estimates and (d) emission trends derived from TDE estimates. Green boxes denote seven regions analyzed in Sect. 3.2. Top-down emission fluxes are computed with Eq. (1) except for IP and EC where Eq. (3) is applied. Linear trends are computed from the time series of annual averages. Dots in (d) represent significant linear trends at the 95 % confidence level.

In addition to the adjustments in average emissions, the TDE also detects changes in NH_3 emissions during the period of 2008-2018, as expressed in linear trends computed from annual time series. We find significant positive emission trends in SA (1.7 Tg a^{-1} decade^{-1} or 18 % decade^{-1}) and TA (2.8 Tg a^{-1} decade^{-1} or 33 % decade^{-1}) (**Fig. 3**). The large positive trends in TA are found around Lake Natron, consistent with Clarisse et al. (2019) (Fig. 2d). These increases in NH_3 emissions are concurrent with intensifying agricultural activities in these regions (Warner et al., 2017; E. Hickman et al., 2020), except for a 2010 peak over SA, which coincides with fires in savanna and evergreen forests there (Chen et al., 2013). Comparison with data from the Food and Agriculture Organization of the United Nations (FAO) (http://www.fao.org/faostat, last access: 7 May 2022) suggests that the increase in SA is driven primarily by growing application of synthetic fertilizer (55 % decade^{-1}), whereas the increase in TA is consistent with increasing manure amount (28 % decade^{-1}) from a growing livestock population (E. Hickman et al., 2021) (**Fig. 4**).

Our results infer large but variable trends over northern high latitudes (e.g., negative trends in Alaska, central Russia, and eastern Europe, but positive trends in Canada) (**Fig. 2d**). Because of large uncertainties associated with high-latitude observations and emission optimization, these trends are less robust but can be partly attributed to variations in fire activities. Decreases in Russia and eastern Europe are related to wildfire of boreal forests in early part of the study period (2008-2011) (Keywood et al., 2012; Warner et al., 2017), while emission increases in Canada is due to wildfire in the late part of the period (2013-2016 and 2017) (Pavlovic et al., 2016), as also shown in the prior fire inventory (GFED4) (**Fig. S4**). We also infer negative trends (-43 % decade^{-1}) in Australia, which are statistically significant, but the absolute magnitude of these trends is small (-0.03 g m^{-2} a^{-1} decade^{-1} in **Fig. 2d**). The TDE estimation does not find significant trends in NH_3 total emissions over the US and Central Asia.
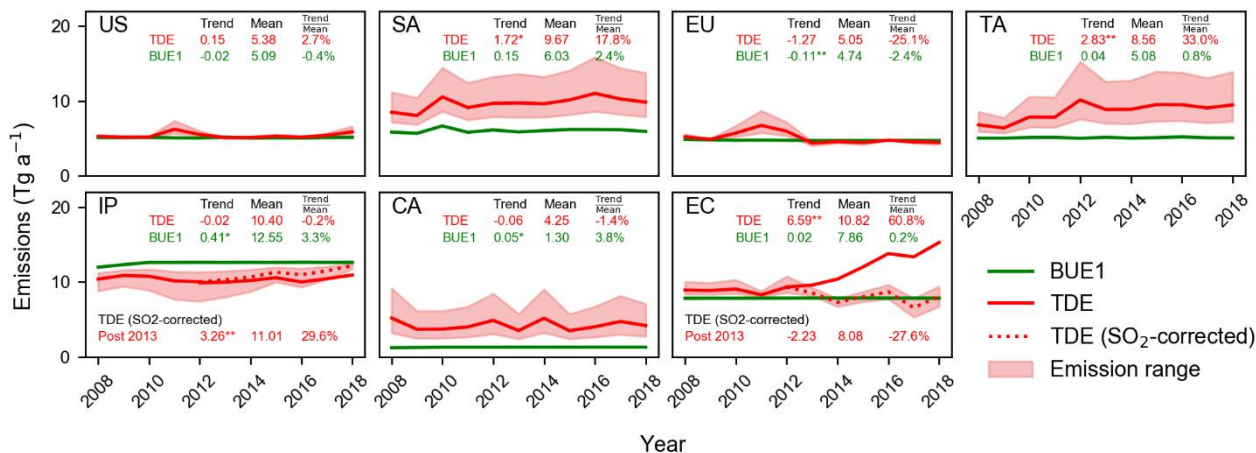
Figure 3. Annual NH₃ emissions for seven selected regions during 2008-2018. Shadings represent the upper and lower bounds derived from uncertainty analyses (see Sect. 2.4). Average annual emissions (Tg a⁻¹), absolute linear trends (Tg a⁻¹ decade⁻¹) and relative trends (% decade⁻¹) for 2008-2018 are inset. The asterisk symbols '*' and '**' represent that linear trends are significant at the 95 % and 99 % confidence level, respectively. Red dashed lines represent top-down NH₃ emission estimates over IP and EC during 2013-2018, based on Eq. (3) that accounts for observed trends of SO₂ (denoted as "SO₂-corrected"). Statistics for this estimate are also inset. The prior inventory (BUE1) implemented in our simulation only partially account for inter-annual changes from bottom-up information (i.e., **Fig. 4**).
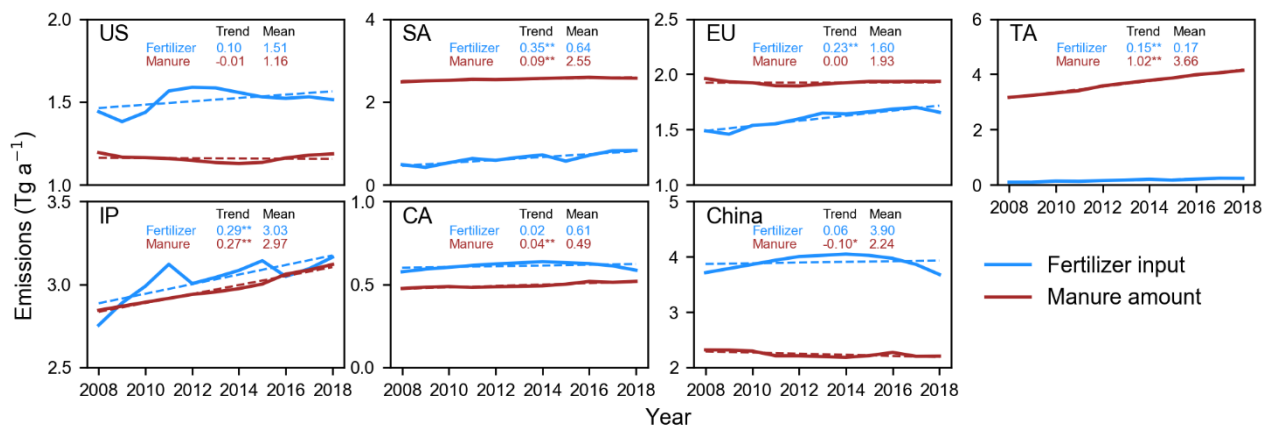
Figure 4. Synthetic fertilizer and livestock manure amount based on FAO reports (http://www.fao.org/faostat) during 2008-2018. To roughly compare the contribution from the two sectors, we convert FAO reported statistics to NH₃ emissions (Tg a⁻¹) by applying fixed emission factors of 13 % for manure N contents (Ma et al., 2020) and 17 % for synthetic fertilizer N contents (Riddick et al., 2016). Values of means (Tg a⁻¹) and linear trends (Tg a⁻¹ decade⁻¹) are inset. Scales differ between panels.

3.3 Impact of changing SO₂ emissions on NH₃ emission trends over eastern China and India

Based on NH₃ column measurements (**Eq. (1)**), we also find a decadal increase of 61 % decade⁻¹ (6.6 Tg a⁻¹ decade⁻¹) in NH₃ emissions over eastern China (**Fig. 3**). This increase is especially large after 2013 and is driven mainly by increases of IASI NH₃ column concentration in eastern China (**Fig. 1c**). This large post-2013 increase is inconsistent with flat or even declining fertilizer input and manure amount (**Fig. 4**). On the other hand, we find no appreciable emission trend in IP (**Fig.**

274   3), which appears to agree with relatively stable IASI NH_3 concentrations over the period (**Fig. 1c**) but is not supported by

275   increases in fertilizer applications and manure amount shown in the FAO report (**Fig. 4**).

276   An assumption underlying **Eq. (1)** is that the model simulation captures the partition between gas-phase NH_3 and aerosol-

277   phase NH_4^+. In addition to alkaline NH_3, the partition is also determined by the abundance of acids (e.g., H_2SO_4 and HNO_3).

278   Inaccurate emissions of their precursors (e.g., SO_2 and NO_2) in the model simulation, in particular over regions with

279   excessive NH_3, can lead to biases in simulating the NH_3-NH_4^+ partition. It is well known that SO_2 emissions in China have

280   decreased rapidly after 2013 because of stringent air pollution control measures (Sun et al., 2018; Zhai et al., 2021), while

281   SO_2 emissions from India have been increasing (Qu et al., 2019). But these regional trends are not captured in our prior

282   simulation because our simulation does not have annual-varying emission inventories for these regions (**Fig. S2**).

283   We find that the discrepancies between top-down (**Eq. 1**) and bottom-up estimates of emission trends over EC and IP can be

284   largely reconciled by including observed SO_2 column concentrations in the top-down calculation (**Eq. (3)**). By accounting

285   for OMI and OMPS observed SO_2 trends (Wang and Wang, 2020), we derive an overall decreasing trend in NH_3 emissions

286   in EC between 2013 and 2018 (-2.2 $\pm$ 2.3 Tg a^{-1} decade^{-1}, -28 $\pm$ 32 % decade^{-1}) (uncertainty derived by perturbing ω by 1%

287   a^{-1}, same for the India results below). This result suggests that observed increases in NH_3 columns over China are largely

288   explained by decreases in SO_2 emissions (**Fig. 1** and **Fig. 3**), consistent with previous studies (Fu et al., 2017; Liu et al.,

289   2018; Lachatre et al., 2019; Chen et al., 2021a). Bottom-up inventories (e.g., MEIC v1.3, EDGAR v5.0) also report stable or

290   declining NH_3 emissions from China during the period (Li et al., 2017; Crippa et al., 2020). Meanwhile, the revised method

291   (**Eq. (3)**) finds a positive post-2013 trend (3.3 $\pm$ 0.3 Tg a^{-1} decade^{-1}, 30 $\pm$ 3 % yr^{-1}) in NH_3 emissions over India. Compared

292   with our original estimate using **Eq. (1)**, NH_3 emission trends derived with **Eq. (3)** (i.e., decrease in China and increase in

293   India after 2013) is more consistent with the bottom-up information of fertilizer input and manure management (**Fig. 4**). This

294   result demonstrates the potential of assimilating both NH_3 and SO_2 satellite observations in constraining NH_3 emissions,

295   which should be further explored in the future.

296   **3.4 Global total NH_3 emissions**

297   Integrating over land areas globally, our IASI-based TDE estimates of NH_3 is 78 (70-92) Tg a^{-1} (range of estimates from

298   uncertainty analysis, see **Table 1**) (**Fig. 5**). This result is about 20-40 % higher than bottom-up inventories (BUE1, 62 Tg a^{-1}

299   and BUE2, 56 Tg a^{-1}). In contrast, a previous study by Evangeliou et al. (2021) also based on the IASI data estimated a much

300   higher global NH_3 emission of 180 Tg a^{-1} (**Fig. 5**). One cause of the difference between the two IASI-based estimates is in

301   diagnosis of NH_3 lifetime from CTM. Evangeliou et al. (2021) treats conversion from NH_3 to NH_4^+ as a terminal loss and

302   diagnoses NH_3 lifetime averaged 11.6 $\pm$ 0.6 h globally from a CTM, which is close to a constant NH_3 lifetime (12 h)

303   assumed in Van Damme et al. (2018). In this study, we account for the fact that fast thermodynamic equilibrium can

304   establish between NH_3 and NH_4^+ so that NH_3 can only be terminally lost through the deposition of the NH_x family (**Eq. (2)**),

305   which yields a global averaged NH_3 lifetime of 21.2 $\pm$ 3.8 h (**Fig. 6**). This longer NH_3 lifetime implies a higher sensitivity of

306   NH_3 column density to NH_3 emissions, leading to a lower estimate for global NH_3 emissions. In addition, instead of locally

307 scaling observed NH₃ column by lifetime (Van Damme et al., 2018; Evangeliou et al, 2021; Marais et al., 2021), our method
308 (**Eq. (1)**) partially accounts for the non-local contribution from transport by including prior NH₃ columns from a full 3-D
309 simulation and using their difference from observed NH₃ columns to correct prior emissions, which prevents derivation of
310 large NH₃ emissions in remote regions where observed NH₃ concentrations are driven mainly by transport. Our data filtering
311 strategy (**Sect 2.1 and 2.2**) is also crucial to avoid spurious top-down results when satellite coverage is poor and the local
312 mass balance assumption does not hold.
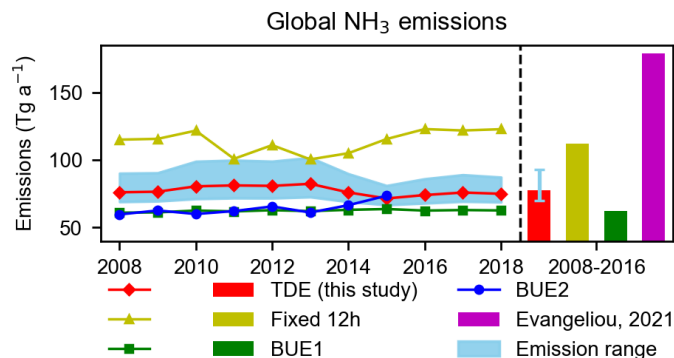
313

314 **Figure 5.** Comparison of our top-down NH₃ emission estimates (TDE) with other top-down (Fixed 12h and Evangeliou et al. (2021)) and
315 bottom-up (BUE1 and BUE2) results during 2008-2018. The red line and red bar represent central estimates of the TDE, and the blue
316 shaded area and the blue error bar indicate the uncertainty evaluated by our study (**Sect. 2.4**).
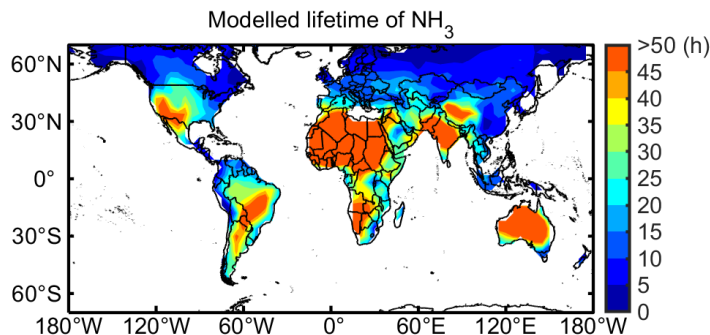
317

318 **Figure 6.** Spatial distribution of NH₃ lifetime (h) diagnosed from GEOS-Chem (Eq. (2)) within the $70°N$-$70°S$ during 2008-2018.

319 **Fig. 6** shows the spatial variation in NH₃ lifetime diagnosed from the GEOS-Chem simulation. Short NH₃ lifetimes (< 10 h)
320 are found mainly in northern high latitudes. Short lifetime in eastern China is due to high wet NH_4^+ deposition velocity,
321 although some regional studies suggested an overestimation of deposition fluxes by the model especially in forest areas (e.g.,
322 Yangtze River basin) (Zhao et al., 2017; Xu et al., 2018). Very long NH₃ lifetime (> 100 h) occurs over Sahara and
323 Australia, where dry conditions result in slow wet deposition.

3.5 Uncertainty evaluation

We derive the uncertainty of top-down estimates from the perturbation tests in **Table 1**. **Fig. 7** shows the global spatial distribution of annual average ~~relative~~ uncertainties of NH$_3$ emissions ~~(ranges~~derived from the ensemble of these perturbation tests ~~divided~~. Absolute uncertainties are expressed as half of the ensemble ranges, and relative uncertainties are computed by ~~their~~normalizing absolute uncertainties by ensemble averages~~). The~~. We find that both absolute and relative uncertainties are large ~~(up to >100%) over northern latitudes,~~ in Central Asia~~, northern~~ and Tropical Africa, ~~and South America, where~~indicating that these source regions are not well constrained by observations ~~are often sparse.~~. In comparison, ~~the relative uncertainties are small (<40 %) in well observed regions including~~observations have some constraints over important source regions of eastern China~~,~~ and northern India, which have small relative uncertainties (< 20 %) but still appreciable absolute uncertainties (> 0.4 g a^{-1} m^{-2}). Uncertainties are small (< 20 % and/or < 0.2 g a^{-1} m^{-2}) in Europe~~,~~ and the U.S.
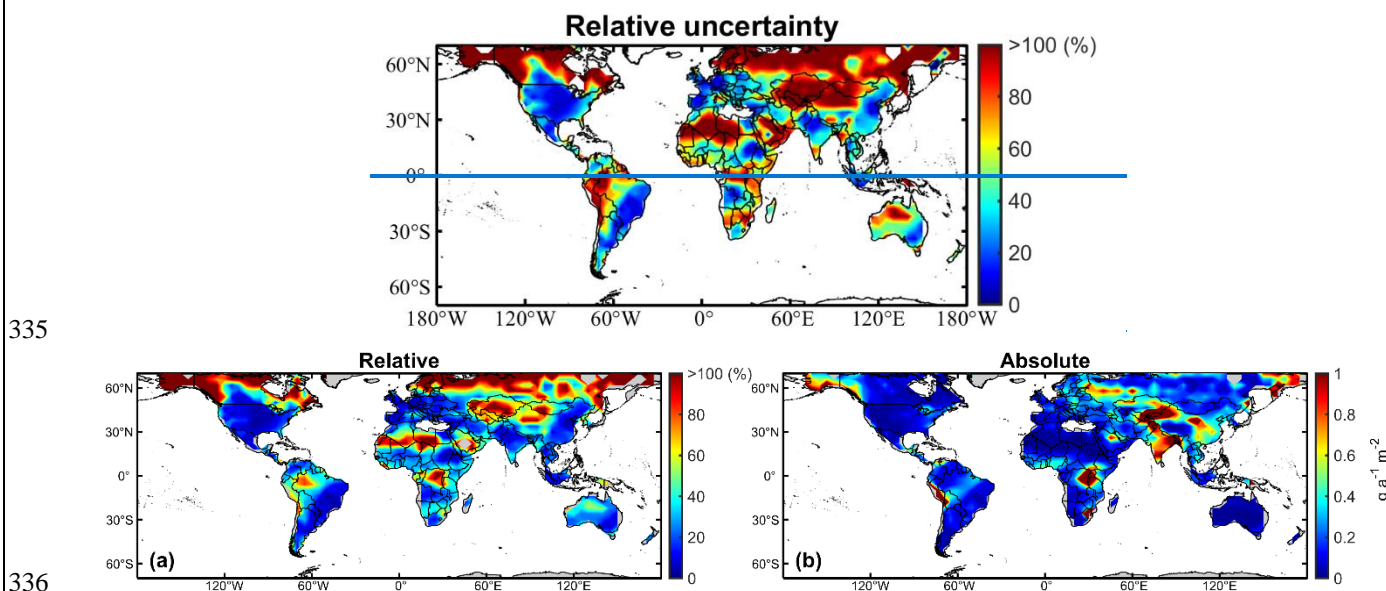
Figure 7. Spatial distribution of TDE (a) relative and (b) absolute uncertainty during 2008-2018. Absolute uncertainties are derived as ~~the discrepancy~~half of ~~emission estimations in parameters~~ the perturbation ensemble range (**Table 1**) ~~divided~~and relative uncertainties are computed by ~~the TDE average during 2008-2018.~~normalizing absolute uncertainties with ensemble averages.

Our fast top-down method (Eq. (1) and Eq. (3)) relies on simplification of NH$_3$ chemical and physical processes. Therefore, it is not guaranteed that a simulation driven by TDE will generate results in improved agreement with IASI observations. We evaluate the consistency of our results using full GEOS-Chem simulations in the selected years of 2008, 2013, and 2018. Results are shown in **Fig. S5** (fractional bias, FB) and **Table S1** (number of valid grid cells, R^2, and root mean square error). The GEOS-Chem simulations driven by the prior emissions (BUE1) tends to underestimate NH$_3$ column density (mean FB ~-30%), while that driven by our TDE estimates achieves lower biases (mean FB ~10%), demonstrating the consistency of our TDE results with IASI observations.

3.6 Comparison to independent surface networks

We also compare simulated surface NH$_3$ concentrations with independent ground-based measurements from, including (1) biweekly averaged NH$_3$ concentrations in North America (AMoN, https://nadp.slh.wisc.edu/networks/ammonia-monitoring-network/, last access: 3 June 2022), Europe(2) half-hourly/daily/weekly averaged NH$_3$ concentrations in (EMEP, http://ebas-data.nilu.no/, last access: 3 June 2022), and South-eastern Asia (EANET, http://ebas-data.nilu.no/, last access: 3 June 2022).(3) monthly averaged NH$_3$ concentrations in south-eastern Asia (EANET, https://www.eanet.asia/, last access: 3 June 2022). AMoN measures NH$_3$ concentrations by passive devices (simple diffusion-type simpler), while EMEP and EANET use both active and passive sampler systems among different sites (multi-type samplers). For comparison, we convert the observed NH$_3$ concentrations in µg m^{-3} to ppbv using a factor of 1.44 (assume 25 °C temperature and 1 atmosphere pressure) and average observations monthly over the GEOS-Chem 4° × 5° grid. **Fig. 8** shows the comparison by season. Only small adjustments are inferred by our satellite-based estimations in these regions (i.e., North America, Europe, and South-eastern Asia). Thus, TDE and BUE1 show similar performance against these ground measurements. Although the simulation can capture the site-to-site variations reasonably well, simulated surface values are in general biased low compared to observations. This low bias is also reported in the evaluation of previous IASI-based estimates (e.g., Evangeliou et al, 2021; Chen et al., 2021b), which may be due). Further investigations are needed to severalunderstand the reasons, for instance, systematic differences between satellite and surface measurementsthis bias.

363

364
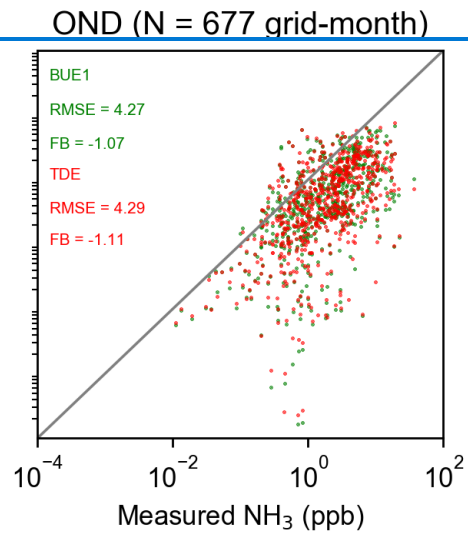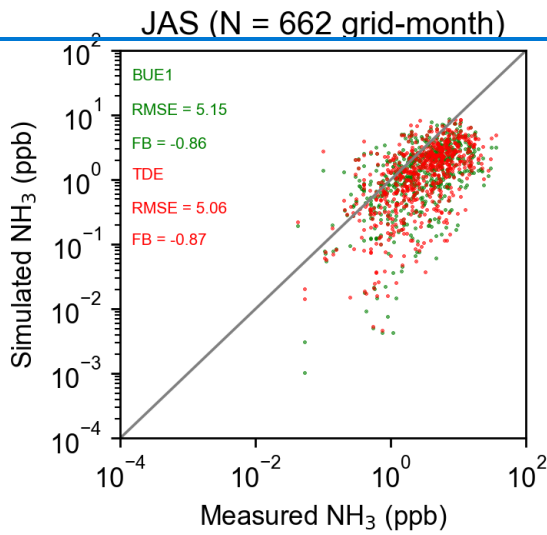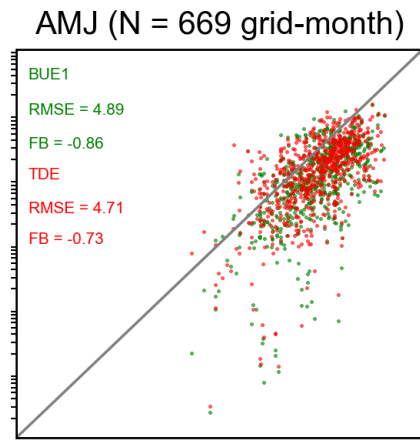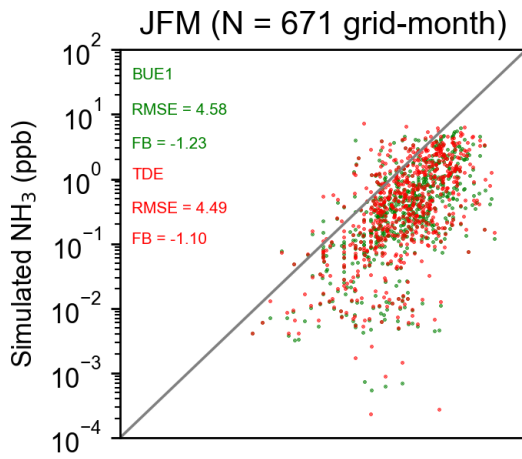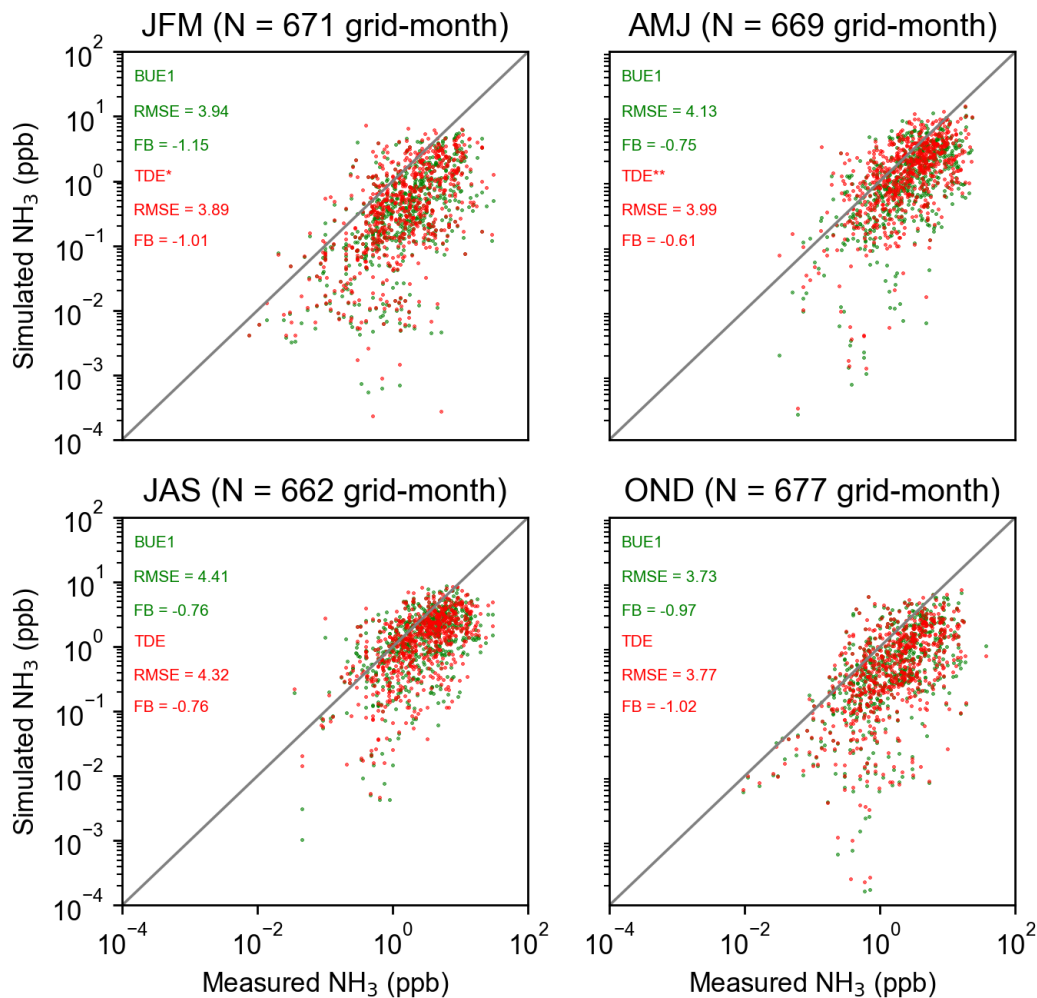
Figure 8. Validation of simulated NH$_3$ concentrations driven by BUE1 and TDE against ground-based measurements from AMoN, EMEP, EANET for selected years (2008, 2013 and 2018) in four seasons (January-March, JFM; April-June, AMJ; July-September, JAS; October-December, OND). Scatterplots are plotted in log scale and average RMSE (ppb) and FB (%) for each season are inset. The asterisk symbols '*' and '**' represent that differences between BUE1 and TDE are significant at the 95 % and 99 % confidence level.

4 Conclusions

This study quantifies global ammonia (NH$_3$) fluxes monthly from 2008 to 2018 at 4° × 5° resolution, through a fast top-down method that incorporates IASI satellite observations and GEOS-Chem model simulations. The top-down method updates the prior NH$_3$ emissions with a correction term positively proportional to the difference of the observed and simulated NH$_3$ concentrations, and inversely proportional to the lifetime diagnosed from a CTM. This method revises previously proposed fast top-down methods in two aspects. First, we account for thermodynamic equilibrium within the NH$_x$ family in diagnosing NH$_3$ lifetime, while previous studies either assume a globally constant lifetime or treat conversion from

376 NH$_3$ to NH$_4^+$ as a terminal sink. Second, our formulation linearizes the column-emission relationship at prior emissions as

377 opposed to zero emissions in the previous method, which in general reduces errors from the local mass balance

378 approximation. Another improvement is that we apply several data filtering procedures to exclude unreliable top-down

379 results that are not sufficiently constrained by observations or affected by large deviations from the local mass balance

380 assumption. The top-down method developed in this study is particularly useful for long-term global analysis of emission

381 trends, because it largely accounts for the impact of meteorology through the CTM simulation and requires only small

382 amount of computation relative to a full-fledged inversion.

383 We apply this improved fast top-down method to IASI NH$_3$ column observations from 2008 to 2018. We find that the BUE1

384 underestimates NH$_3$ emission over South America (62 %) and tropical Africa (69 %), but overestimates over India (14 %)

385 and Canada (33 %). The bottom-up inventory agrees with the top-down estimate over the U.S., Europe, and eastern China

386 (i.e., within 10 %). Our analysis also shows significant increases in India (13 % decade^{-1}), tropical Africa (33 % decade^{-1}),

387 and South America (18 % decade^{-1}) during the study period, consistent with intensifying agricultural activities over these

388 regions. An analysis of agricultural statistics suggests that the increase in tropical Africa is likely driven by growing

389 livestock population and that in South America by increasing fertilizer usage.

390 We show that large increases in NH$_3$ concentrations in eastern China is mainly driven by rapid decreases in SO$_2$ emissions in

391 recent years. By accounting for observed SO$_2$ columns, we find that NH$_3$ emissions from eastern China are significantly

392 decreasing during 2008-2018 (-19 % decade^{-1}), with a larger negative trend after 2013 (-28 % decade^{-1}), as compared to a

393 significant positive trend (61 % decade^{-1}) derived from assimilating only NH$_3$ data. Similarly, a lack of trend in observed

394 NH$_3$ concentrations over India is due to concurrent increases in SO$_2$ and NH$_3$ emissions. After including observed SO$_2$

395 columns in the calculation, we estimate a 13 % increase in NH$_3$ emissions over India, with a significant post-2013 positive

396 trend (30 % decade^{-1}). These results from assimilating both NH$_3$ and SO$_2$ data is more consistent with the agricultural

397 statistics in China and India. The multi-satellite (SO$_2$ and NH$_3$) method is only applied in India and China in this study. To

398 extend this idea globally requires development of formulations for varied sulfate-nitrate-ammonium aerosol regimes and

399 needs to be addressed in a future study.

400 Our estimate for global total NH$_3$ emission is 78 (70-92) Tg a^{-1}, about 30 % higher than the BUE1 estimate. This contrasts

401 with a much higher estimate (180 Tg a^{-1}) derived from Evangeliou et al. (2021) also using IASI data. The discrepancy can be

402 primarily attributed to a longer NH$_3$ lifetime (i.e., global average 21 h) diagnosed in our method, which represents a greater

403 sensitivity of NH$_3$ column to emissions, and a more conservative data filtering strategy, which removes potentially unreliable

404 top-down results. Our diagnosis of NH$_3$ lifetime is an improvement over Evangeliou et al. (2021), by accounting for the

405 thermodynamic equilibrium between gas phase NH$_3$ and aerosol phase NH$_4^+$ in our formula. We show with model

406 simulations, our top-down estimate achieves better consistency with IASI observations, compared to the bottom-up emission

407 inventory.

408

409 *Data availability.*

410 The IASI L2 ammonia satellite observations are available at the AERIS data infrastructure (https://iasi.aeris-data.fr/). The

411 ERA5 skin temperature and GFAS fire emission can be request through Copernicus Climate Data Store

412 (https://cds.climate.copernicus.eu/cdsapp#!/home). Agricultural data are available through Food and Agriculture

413 Organization of the United Nations (FAO) (http://www.fao.org/faostat). The GEOS-Chem model can be retrieved from

414 10.5281/zenodo.3974569. All the other data and scripts used for the present publication are available under MIT license on

415 GitHub: https://github.com/bnulzq/NH3-emission.git and can be obtained from corresponding author upon request.

416 *Author contributions.*

417 ZL and YZ designed the study. ZL performed the simulations and analyses and wrote and coordinated the paper. WC

418 contributed to the model simulations for consistency evaluation. LC, MVD, and PFC developed the IASI-NH3 satellite

419 product. ZL and YZ wrote the paper with inputs from all authors.

420 *Competing interests*

421 The contact author has declared that neither they nor their co-authors have any competing interests.

422 *Acknowledgements.*

423 This study is supported by Westlake University. We thank the High-Performance Computing Center of Westlake University

424 for the facility support and technical assistance. We acknowledge the AERIS data infrastructure https://www.aeris-data.fr for

425 providing access to the IASI data. The IASI L1c data are received through the EUMETCast near real-time data distribution

426 service. Research at ULB was supported by the Belgian State Federal Office for Scientific, Technical and Cultural Affairs

427 (Prodex HIRS) and the Air Liquide Foundation (TAPIR project). LC is Research Associate supported by the Belgian F.R.S.-

428 FNRS. Hersbach et al., (2020) was downloaded from the Copernicus Climate Change Service (C3S) Climate Data Store. The

429 results contain modified Copernicus Climate Change Service information 2020. Neither the European Commission nor

430 ECMWF is responsible for any use that may be made of the Copernicus information or data it contains. IASI is a join

431 mission of Eumetsat and the "Centre National d'Études Spatiales" (CNES, France). We acknowledge the constructive

432 comments and suggestions from Prof. Peter Hess from the Cornell University, Dr. Yi Wang from the University of Iowa, and

433 Dr. Shixian Zhai from Harvard University. We also acknowledge Dr. Nikolaos Evangeliou from Norwegian Institute for Air

434 Research for providing his NH$_3$ emission flux data and for discussions with ZL.

References

Acharja, P., Ali, K., Ghude, S. D., Sinha, V., Sinha, B., Kulkarni, R., Gultepe, I., and Rajeevan, M. N.: Enhanced secondary aerosol formation driven by excess ammonia during fog episodes in Delhi, India, Chemosphere, 289, 133155, 10.1016/j.chemosphere.2021.133155, 2022.

Amos, H. M., Jacob, D. J., Holmes, C. D., Fisher, J. A., Wang, Q., Yantosca, R. M., Corbitt, E. S., Galarneau, E., Rutter, A. P., Gustin, M. S., Steffen, A., Schauer, J. J., Graydon, J. A., Louis, V. L. S., Talbot, R. W., Edgerton, E. S., Zhang, Y., and Sunderland, E. M.: Gas-particle partitioning of atmospheric Hg(II) and its effect on global mercury deposition, Atmospheric Chemistry and Physics, 12, 591-603, 10.5194/acp-12-591-2012, 2012.

Behera, S. N., Sharma, M., Aneja, V. P., and Balasubramanian, R.: Ammonia in the atmosphere: a review on emission sources, atmospheric chemistry and deposition on terrestrial bodies, Environ Sci Pollut Res Int, 20, 8092-8131, 10.1007/s11356-013-2051-9, 2013.

Bey, I., Jacob, D. J., Yantosca, R. M., Logan, J. A., Field, B. D., Fiore, A. M., Li, Q., Liu, H. Y., Mickley, L. J., and Schultz, M. G.: Global modeling of tropospheric chemistry with assimilated meteorology: Model description and evaluation, Journal of Geophysical Research: Atmospheres, 106, 23073-23095, 10.1029/2001jd000807, 2001.

Bouwman, A. F., Lee, D. S., Asman, W. A. H., Dentener, F. J., Van Der Hoek, K. W., and Olivier, J. G. J.: A global high-resolution emission inventory for ammonia, Global Biogeochemical Cycles, 11, 561-587, 10.1029/97gb02266, 1997.

Cao, H., Henze, D. K., Shephard, M. W., Dammers, E., Cady-Pereira, K., Alvarado, M., Lonsdale, C., Luo, G., Yu, F., Zhu, L., Danielson, C. G., and Edgerton, E. S.: Inverse modeling of NH3 sources using CrIS remote sensing measurements, Environmental Research Letters, 15, 10.1088/1748-9326/abb5cc, 2020.

Chen, Y., Morton, D. C., Jin, Y., Collatz, G. J., Kasibhatla, P. S., van der Werf, G. R., DeFries, R. S., and Randerson, J. T.: Long-term trends and interannual variability of forest, savanna and agricultural fires in South America, Carbon Management, 4, 617-638, 10.4155/cmt.13.61, 2014.

Chen, Y., Zhang, L., Henze, D. K., Zhao, Y., Lu, X., Winiwarter, W., Guo, Y., Liu, X., Wen, Z., Pan, Y., and Song, Y.: Interannual variation of reactive nitrogen emissions and their impacts on PM2.5 air pollution in China during 2005–2015, Environmental Research Letters, 16, 10.1088/1748-9326/ac3695, 2021a.

Chen, Y., Shen, H., Kaiser, J., Hu, Y., Capps, S. L., Zhao, S., Hakami, A., Shih, J.-S., Pavur, G. K., Turner, M. D., Henze, D. K., Resler, J., Nenes, A., Napelenok, S. L., Bash, J. O., Fahey, K. M., Carmichael, G. R., Chai, T., Clarisse, L., Coheur, P.-F., Van Damme, M., and Russell, A. G.: High-resolution hybrid inversion of IASI ammonia columns to constrain US ammonia emissions using the CMAQ adjoint model, Atmospheric Chemistry and Physics, 21, 2067-2082, 10.5194/acp-21-2067-2021, 2021b.

471 Clarisse, L., Van Damme, M., Gardner, W., Coheur, P. F., Clerbaux, C., Whitburn, S., ... & Hurtmans,
472 D. (2019). Atmospheric ammonia (NH_3) emanations from Lake Natron's saline mudflats. Scientific
473 reports, 9(1), 1-12.

474 Clerbaux, C., Boynard, A., Clarisse, L., George, M., Hadji-Lazaro, J., Herbin, H., Hurtmans, D.,
475 Pommier, M., Razavi, A., Turquety, S. J. A. C., and Physics: Monitoring of atmospheric composition
476 using the thermal infrared IASI/MetOp sounder, Atmospheric Chemistry and Physics, 9, 6041-6054,
477 2009.

478 Crippa, M., Solazzo, E., Huang, G., Guizzardi, D., Koffi, E., Muntean, M., Schieberle, C., Friedrich, R.,
479 and Janssens-Maenhout, G.: High resolution temporal profiles in the Emissions Database for Global
480 Atmospheric Research, Sci Data, 7, 121, 10.1038/s41597-020-0462-2, 2020.

481 Dirnbock, T., Grandin, U., Bernhardt-Romermann, M., Beudert, B., Canullo, R., Forsius, M., Grabner,
482 M. T., Holmberg, M., Kleemola, S., Lundin, L., Mirtl, M., Neumann, M., Pompei, E., Salemaa, M.,
483 Starlinger, F., Staszewski, T., and Uzieblo, A. K.: Forest floor vegetation response to nitrogen
484 deposition in Europe, Glob Chang Biol, 20, 429-440, 10.1111/gcb.12440, 2014.

485 Erisman, J. W. J. S.: How ammonia feeds and pollutes the world, Science, 374, 685-686, 2021.

486 Evangeliou, N., Balkanski, Y., Eckhardt, S., Cozic, A., Van Damme, M., Coheur, P.-F., Clarisse, L.,
487 Shephard, M. W., Cady-Pereira, K. E., and Hauglustaine, D.: 10-year satellite-constrained fluxes of
488 ammonia improve performance of chemistry transport models, Atmospheric Chemistry and Physics, 21,
489 4431-4451, 10.5194/acp-21-4431-2021, 2021.

490 Fountoukis, C., Nenes, A. J. A. C., and Physics: ISORROPIA II: a computationally efficient
491 thermodynamic equilibrium model for K+–Ca 2+–Mg 2+–NH 4+–Na+–SO 4 2−–NO 3−–Cl−–H 2 O
492 aerosols, Atmospheric Chemistry and Physics, 7, 4639-4659, 2007.

493 Franco, B., Clarisse, L., Stavrakou, T., Müller, J. F., Van Damme, M., Whitburn, S., Hadji-Lazaro, J.,
494 Hurtmans, D., Taraborrelli, D., Clerbaux, C., and Coheur, P. F.: A General Framework for Global
495 Retrievals of Trace Gases From IASI: Application to Methanol, Formic Acid, and PAN, Journal of
496 Geophysical Research: Atmospheres, 123, 10.1029/2018jd029633, 2018.

497 Fu, X., Wang, S., Xing, J., Zhang, X., Wang, T., and Hao, J.: Increasing Ammonia Concentrations
498 Reduce the Effectiveness of Particle Pollution Control Achieved via SO2 and NOX Emissions
499 Reduction in East China, Environmental Science & Technology Letters, 4, 221-227,
500 10.1021/acs.estlett.7b00143, 2017.

501 Gelaro, R., McCarty, W., Suarez, M. J., Todling, R., Molod, A., Takacs, L., Randles, C., Darmenov, A.,
502 Bosilovich, M. G., Reichle, R., Wargan, K., Coy, L., Cullather, R., Draper, C., Akella, S., Buchard, V.,
503 Conaty, A., da Silva, A., Gu, W., Kim, G. K., Koster, R., Lucchesi, R., Merkova, D., Nielsen, J. E.,
504 Partyka, G., Pawson, S., Putman, W., Rienecker, M., Schubert, S. D., Sienkiewicz, M., and Zhao, B.:
505 The Modern-Era Retrospective Analysis for Research and Applications, Version 2 (MERRA-2), J Clim,
506 Volume 30, 5419-5454, 10.1175/JCLI-D-16-0758.1, 2017.

Gu, B., Zhang, L., Van Dingenen, R., Vieno, M., Van Grinsven, H. J., Zhang, X., Zhang, S., Chen, Y., Wang, S., and Ren, C. J. S.: Abating ammonia is more cost-effective than nitrogen oxides for mitigating PM2. 5 air pollution, Science, 374, 758-762, 2021.

Guenther, A. B., Jiang, X., Heald, C. L., Sakulyanontvittaya, T., Duhl, T., Emmons, L. K., and Wang, X.: The Model of Emissions of Gases and Aerosols from Nature version 2.1 (MEGAN2.1): an extended and updated framework for modeling biogenic emissions, Geoscientific Model Development, 5, 1471-1492, 10.5194/gmd-5-1471-2012, 2012.

Guo, X., Wang, R., Pan, D., Zondlo, M. A., Clarisse, L., Van Damme, M., Whitburn, S., Coheur, P. F., Clerbaux, C., Franco, B., Golston, L. M., Wendt, L., Sun, K., Tao, L., Miller, D., Mikoviny, T., Müller, M., Wisthaler, A., Tevlin, A. G., Murphy, J. G., Nowak, J. B., Roscioli, J. R., Volkamer, R., Kille, N., Neuman, J. A., Eilerman, S. J., Crawford, J. H., Yacovitch, T. I., Barrick, J. D., and Scarino, A. J.: Validation of IASI Satellite Ammonia Observations at the Pixel Scale Using In Situ Vertical Profiles, Journal of Geophysical Research: Atmospheres, 126, 10.1029/2020jd033475, 2021.

Hersbach, H., Bell, B., Berrisford, P., Hirahara, S., Horányi, A., Muñoz-Sabater, J., Nicolas, J., Peubey, C., Radu, R., Schepers, D., Simmons, A., Soci, C., Abdalla, S., Abellan, X., Balsamo, G., Bechtold, P., Biavati, G., Bidlot, J., Bonavita, M., Chiara, G., Dahlgren, P., Dee, D., Diamantakis, M., Dragani, R., Flemming, J., Forbes, R., Fuentes, M., Geer, A., Haimberger, L., Healy, S., Hogan, R. J., Hólm, E., Janisková, M., Keeley, S., Laloyaux, P., Lopez, P., Lupu, C., Radnoti, G., Rosnay, P., Rozum, I., Vamborg, F., Villaume, S., and Thépaut, J. N.: The ERA5 global reanalysis, Quarterly Journal of the Royal Meteorological Society, 146, 1999-2049, 10.1002/qj.3803, 2020.

Hickman, J. E., Andela, N., Tsigaridis, K., Galy-Lacaux, C., Ossohou, M., and Bauer, S. E.: Reductions in NO2 burden over north equatorial Africa from decline in biomass burning in spite of growing fossil fuel use, 2005 to 2017, Proc Natl Acad Sci U S A, 118, 10.1073/pnas.2002579118, 2021a.

Hickman, J. E., Andela, N., Dammers, E., Clarisse, L., Coheur, P.-F., Van Damme, M., Di Vittorio, C. A., Ossohou, M., Galy-Lacaux, C., Tsigaridis, K., and Bauer, S. E.: Changes in biomass burning, wetland extent, or agriculture drive atmospheric NH$_3$; trends in select African regions, Atmospheric Chemistry and Physics, 21, 16277-16291, 10.5194/acp-21-16277-2021, 2021b.

Hoesly, R. M., Smith, S. J., Feng, L., Klimont, Z., Janssens-Maenhout, G., Pitkanen, T., Seibert, J. J., Vu, L., Andres, R. J., Bolt, R. M., Bond, T. C., Dawidowski, L., Kholod, N., Kurokawa, J.-i., Li, M., Liu, L., Lu, Z., Moura, M. C. P., O'Rourke, P. R., and Zhang, Q.: Historical (1750–2014) anthropogenic emissions of reactive gases and aerosols from the Community Emissions Data System (CEDS), Geoscientific Model Development, 11, 369-408, 10.5194/gmd-11-369-2018, 2018.

Höpfner, M., Ungermann, J., Borrmann, S., Wagner, R., Spang, R., Riese, M., Stiller, G., Appel, O., Batenburg, A. M., Bucci, S., Cairo, F., Dragoneas, A., Friedl-Vallon, F., Hünig, A., Johansson, S., Krasauskas, L., Legras, B., Leisner, T., Mahnke, C., Möhler, O., Molleker, S., Müller, R., Neubert, T., Orphal, J., Preusse, P., Rex, M., Saathoff, H., Stroh, F., Weigel, R., and Wohltmann, I.: Ammonium

nitrate particles formed in upper troposphere from ground ammonia sources during Asian monsoons, Nature Geoscience, 12, 608-612, 10.1038/s41561-019-0385-8, 2019.

Keywood, M., Kanakidou, M., Stohl, A., Dentener, F., Grassi, G., Meyer, C. P., Torseth, K., Edwards, D., Thompson, A. M., Lohmann, U., and Burrows, J.: Fire in the Air: Biomass Burning Impacts in a Changing Climate, Critical Reviews in Environmental Science and Technology, 43, 40-83, 10.1080/10643389.2011.604248, 2011.

Lachatre, M., Fortems-Cheiney, A., Foret, G., Siour, G., Dufour, G., Clarisse, L., Clerbaux, C., Coheur, P.-F., Van Damme, M., and Beekmann, M.: The unintended consequence of SO_2 and NO_2; regulations over China: increase of ammonia levels and impact on $PM_{2.5}$; concentrations, Atmospheric Chemistry and Physics, 19, 6701-6716, 10.5194/acp-19-6701-2019, 2019.

Li, M., Zhang, Q., Kurokawa, J.-i., Woo, J.-H., He, K., Lu, Z., Ohara, T., Song, Y., Streets, D. G., Carmichael, G. R., Cheng, Y., Hong, C., Huo, H., Jiang, X., Kang, S., Liu, F., Su, H., and Zheng, B.: MIX: a mosaic Asian anthropogenic emission inventory under the international collaboration framework of the MICS-Asia and HTAP, Atmospheric Chemistry and Physics, 17, 935-963, 10.5194/acp-17-935-2017, 2017.

Liu, M., Huang, X., Song, Y., Xu, T., Wang, S., Wu, Z., Hu, M., Zhang, L., Zhang, Q., Pan, Y., Liu, X., and Zhu, T.: Rapid SO_2; emission reductions significantly increase tropospheric ammonia concentrations over the North China Plain, Atmospheric Chemistry and Physics, 18, 17933-17943, 10.5194/acp-18-17933-2018, 2018.

Liu, X., Zhang, Y., Han, W., Tang, A., Shen, J., Cui, Z., Vitousek, P., Erisman, J. W., Goulding, K., Christie, P., Fangmeier, A., and Zhang, F.: Enhanced nitrogen deposition over China, Nature, 494, 459-462, 10.1038/nature11917, 2013.

Ma, R., Zou, J., Han, Z., Yu, K., Wu, S., Li, Z., Liu, S., Niu, S., Horwath, W. R., and Zhu-Barker, X.: Global soil-derived ammonia emissions from agricultural nitrogen fertilizer application: A refinement based on regional and crop-specific emission factors, Glob Chang Biol, 27, 855-867, 10.1111/gcb.15437, 2021.

Ma, X., Yu, F., and Luo, G.: Aerosol direct radiative forcing based on GEOS-Chem-APM and uncertainties, Atmospheric Chemistry and Physics, 12, 5563-5581, 10.5194/acp-12-5563-2012, 2012.

Marais, E. A. and Wiedinmyer, C.: Air Quality Impact of Diffuse and Inefficient Combustion Emissions in Africa (DICE-Africa), Environ Sci Technol, 50, 10739-10745, 10.1021/acs.est.6b02602, 2016.

Marais, E. A., Pandey, A. K., Van Damme, M., Clarisse, L., Coheur, P. F., Shephard, M. W., Cady-Pereira, K. E., Misselbrook, T., Zhu, L., Luo, G., and Yu, F.: UK Ammonia Emissions Estimated With Satellite Observations and GEOS-Chem, Journal of Geophysical Research: Atmospheres, 126, 10.1029/2021jd035237, 2021.

Park, R. J.: Natural and transboundary pollution influences on sulfate-nitrate-ammonium aerosols in the United States: Implications for policy, Journal of Geophysical Research, 109, 10.1029/2003jd004473, 2004.

Paulot, F., Jacob, D. J., Pinder, R. W., Bash, J. O., Travis, K., and Henze, D. K.: Ammonia emissions in the United States, European Union, and China derived by high-resolution inversion of ammonium wet deposition data: Interpretation with a new agricultural emissions inventory (MASAGE_NH3), Journal of Geophysical Research: Atmospheres, 119, 4343-4364, 10.1002/2013jd021130, 2014.

Pavlovic, R., Chen, J., Anderson, K., Moran, M. D., Beaulieu, P. A., Davignon, D., and Cousineau, S.: The FireWork air quality forecast system with near-real-time biomass burning emissions: Recent developments and evaluation of performance for the 2015 North American wildfire season, J Air Waste Manag Assoc, 66, 819-841, 10.1080/10962247.2016.1158214, 2016.

Qu, Z., Henze, D. K., Li, C., Theys, N., Wang, Y., Wang, J., Wang, W., Han, J., Shim, C., Dickerson, R. R., and Ren, X.: SO2 Emission Estimates Using OMI SO2 Retrievals for 2005-2017, J Geophys Res Atmos, 124, 8336-8359, 10.1029/2019JD030243, 2019.

Riddick, S., Ward, D., Hess, P., Mahowald, N., Massad, R., and Holland, E.: Estimate of changes in agricultural terrestrial nitrogen pathways and ammonia emissions from 1850 to present in the Community Earth System Model, Biogeosciences, 13, 3397-3426, 10.5194/bg-13-3397-2016, 2016.

Schiferl, L. D., Heald, C. L., Van Damme, M., Clarisse, L., Clerbaux, C., Coheur, P.-F., Nowak, J. B., Neuman, J. A., Herndon, S. C., Roscioli, J. R., and Eilerman, S. J.: Interannual variability of ammonia concentrations over the United States:

sources and implications, Atmospheric Chemistry and Physics, 16, 12305-12328, 10.5194/acp-16-12305-2016, 2016.

Stevens, C. J., Dupre, C., Dorland, E., Gaudnik, C., Gowing, D. J., Bleeker, A., Diekmann, M., Alard, D., Bobbink, R., Fowler, D., Corcket, E., Mountford, J. O., Vandvik, V., Aarrestad, P. A., Muller, S., and Dise, N. B.: Nitrogen deposition threatens species richness of grasslands across Europe, Environ Pollut, 158, 2940-2945, 10.1016/j.envpol.2010.06.006, 2010.

Sun, W., Shao, M., Granier, C., Liu, Y., Ye, C. S., and Zheng, J. Y.: Long-Term Trends of Anthropogenic SO2, NOx, CO, and NMVOCs Emissions in China, Earth's Future, 6, 1112-1133, 10.1029/2018ef000822, 2018.

Sutton, M. A., Reis, S., Riddick, S. N., Dragosits, U., Nemitz, E., Theobald, M. R., Tang, Y. S., Braban, C. F., Vieno, M., Dore, A. J., Mitchell, R. F., Wanless, S., Daunt, F., Fowler, D., Blackall, T. D., Milford, C., Flechard, C. R., Loubet, B., Massad, R., Cellier, P., Personne, E., Coheur, P. F., Clarisse, L., Van Damme, M., Ngadi, Y., Clerbaux, C., Skjoth, C. A., Geels, C., Hertel, O., Wichink Kruit, R. J., Pinder, R. W., Bash, J. O., Walker, J. T., Simpson, D., Horvath, L., Misselbrook, T. H., Bleeker, A., Dentener, F., and de Vries, W.: Towards a climate-dependent paradigm of ammonia emission and deposition, Philos Trans R Soc Lond B Biol Sci, 368, 20130166, 10.1098/rstb.2013.0166, 2013.

613 Van Damme, M., Whitburn, S., Clarisse, L., Clerbaux, C., Hurtmans, D., and Coheur, P.-F.: Version 2
614 of the IASI NH$_3$; neural network retrieval algorithm: near-real-time and reanalysed datasets,
615 Atmospheric Measurement Techniques, 10, 4905-4914, 10.5194/amt-10-4905-2017, 2017.

616 Van Damme, M., Clarisse, L., Whitburn, S., Hadji-Lazaro, J., Hurtmans, D., Clerbaux, C., and Coheur,
617 P. F.: Industrial and agricultural ammonia point sources exposed, Nature, 564, 99-103, 10.1038/s41586-
618 018-0747-1, 2018.

619 Van Damme, M., Clarisse, L., Heald, C. L., Hurtmans, D., Ngadi, Y., Clerbaux, C., Dolman, A. J.,
620 Erisman, J. W., and Coheur, P. F.: Global distributions, time series and error characterization of
621 atmospheric ammonia (NH$_3$) from IASI satellite observations, Atmospheric Chemistry and Physics, 14,
622 2905-2922, 10.5194/acp-14-2905-2014, 2014.

623 Van Damme, M., Clarisse, L., Franco, B., Sutton, M. A., Erisman, J. W., Wichink Kruit, R., van
624 Zanten, M., Whitburn, S., Hadji-Lazaro, J., Hurtmans, D., Clerbaux, C., and Coheur, P.-F.: Global,
625 regional and national trends of atmospheric ammonia derived from a decadal (2008–2018) satellite
626 record, Environmental Research Letters, 16, 10.1088/1748-9326/abd5e0, 2021.

627 Van Damme, M., Clarisse, L., Dammers, E., Liu, X., Nowak, J. B., Clerbaux, C., Flechard, C. R., Galy-
628 Lacaux, C., Xu, W., Neuman, J. A., Tang, Y. S., Sutton, M. A., Erisman, J. W., and Coheur, P. F.:
629 Towards validation of ammonia (NH$_3$) measurements from the IASI satellite, Atmospheric
630 Measurement Techniques, 8, 1575-1591, 10.5194/amt-8-1575-2015, 2015.

631 van der Graaf, S., Dammers, E., Segers, A., Kranenburg, R., Schaap, M., Shephard, M. W., and
632 Erisman, J. W.: Data assimilation of CrIS NH$_3$; satellite observations for improving spatiotemporal
633 NH$_3$; distributions in LOTOS-EUROS, Atmospheric Chemistry and Physics, 22, 951-972, 10.5194/acp-
634 22-951-2022, 2022.

635 van der Werf, G. R., Randerson, J. T., Giglio, L., van Leeuwen, T. T., Chen, Y., Rogers, B. M., Mu, M.,
636 van Marle, M. J. E., Morton, D. C., Collatz, G. J., Yokelson, R. J., and Kasibhatla, P. S.: Global fire
637 emissions estimates during 1997–2016, Earth System Science Data, 9, 697-720, 10.5194/essd-9-697-
638 2017, 2017.

639 Vira, J., Hess, P., Ossohou, M., and Galy-Lacaux, C., 10.5194/acp-2021-538,

640 Wang, Q., Jacob, D. J., Fisher, J. A., Mao, J., Leibensperger, E. M., Carouge, C. C., Le Sager, P.,
641 Kondo, Y., Jimenez, J. L., Cubison, M. J., and Doherty, S. J.: Sources of carbonaceous aerosols and
642 deposited black carbon in the Arctic in winter-spring: implications for radiative forcing, Atmospheric
643 Chemistry and Physics, 11, 12453-12473, 10.5194/acp-11-12453-2011, 2011.

644 Wang, Y. and Wang, J.: Tropospheric SO2 and NO2 in 2012–2018: Contrasting views of two sensors
645 (OMI and OMPS) from space, Atmospheric Environment, 223, 10.1016/j.atmosenv.2019.117214, 2020.

646 Warner, J. X., Dickerson, R. R., Wei, Z., Strow, L. L., Wang, Y., and Liang, Q.: Increased atmospheric
647 ammonia over the world's major agricultural areas detected from space, Geophys Res Lett, 44, 2875-
648 2884, 10.1002/2016GL072305, 2017.

649 Wesely, M.: Parameterization of surface resistances to gaseous dry deposition in regional-scale
650 numerical models☆, Atmospheric Environment, 41, 52-63, 10.1016/j.atmosenv.2007.10.058, 2007.

651 Whitburn, S., Van Damme, M., Clarisse, L., Bauduin, S., Heald, C. L., Hadji-Lazaro, J., Hurtmans, D.,
652 Zondlo, M. A., Clerbaux, C., and Coheur, P. F.: A flexible and robust neural network IASI-
653 NH3retrieval algorithm, Journal of Geophysical Research: Atmospheres, 121, 6581-6599,
654 10.1002/2016jd024828, 2016.

655 Xu, W., Zhao, Y., Liu, X., Dore, A. J., Zhang, L., Liu, L., and Cheng, M.: Atmospheric nitrogen
656 deposition in the Yangtze River basin: Spatial pattern and source attribution, Environ Pollut, 232, 546-
657 555, 10.1016/j.envpol.2017.09.086, 2018.

658 Zhai, S., Jacob, D. J., Wang, X., Liu, Z., Wen, T., Shah, V., Li, K., Moch, J. M., Bates, K. H., Song, S.,
659 Shen, L., Zhang, Y., Luo, G., Yu, F., Sun, Y., Wang, L., Qi, M., Tao, J., Gui, K., Xu, H., Zhang, Q.,
660 Zhao, T., Wang, Y., Lee, H. C., Choi, H., and Liao, H.: Control of particulate nitrate air pollution in
661 China, Nature Geoscience, 14, 389-395, 10.1038/s41561-021-00726-z, 2021.

662 Zhang, L., Chen, Y., Zhao, Y., Henze, D. K., Zhu, L., Song, Y., Paulot, F., Liu, X., Pan, Y., Lin, Y., and
663 Huang, B.: Agricultural ammonia emissions in China: reconciling bottom-up and top-down estimates,
664 Atmospheric Chemistry and Physics, 18, 339-355, 10.5194/acp-18-339-2018, 2018.

665 Zhang, X., Wu, Y., Liu, X., Reis, S., Jin, J., Dragosits, U., Van Damme, M., Clarisse, L., Whitburn, S.,
666 Coheur, P. F., and Gu, B.: Ammonia Emissions May Be Substantially Underestimated in China,
667 Environ Sci Technol, 51, 12089-12096, 10.1021/acs.est.7b02171, 2017.

668 Zhao, Y., Duan, L., Xing, J., Larssen, T., Nielsen, C. P., and Hao, J.: Soil acidification in China: is
669 controlling SO2 emissions enough?, 2009.

670 Zhao, Y., Zhang, L., Chen, Y., Liu, X., Xu, W., Pan, Y., and Duan, L.: Atmospheric nitrogen deposition
671 to China: A model analysis on nitrogen budget and critical load exceedance, Atmospheric Environment,
672 153, 32-40, 10.1016/j.atmosenv.2017.01.018, 2017.

673